PEER REVIEWED

Finite Element Modeling of Single-Particle Impacts for the Optimization of Antimicrobial Copper Cold Spray Coatings

Kristin Sundberg[1] · Bryer C. Sousa[2] · Jeremy Schreiber[3] · Caitlin E. Walde[4] · Timothy J. Eden[3] · Richard D. Sisson Jr.[2] · Danielle L. Cote[2]

Abstract Prior work has demonstrated greater anti-pathogenic efficacy concerning the nanostructured copper cold spray coatings versus conventional copper cold spray coatings, while both the nanostructured and conventional cold spray coatings maintain greater contact killing/inactivation rates relative to other thermal spray deposition methods. Recent work has more heavily focused upon the nanostructured cold spray coatings greater efficacy. However, the antimicrobial efficacy of conventional copper cold spray coatings may be improved upon by way of identifying processing parameters that yield microstructures with the greatest concentration of atomic copper ion diffusion pathways. Since ideal processing parameters for a given application can be computed in silico via finite element analysis methods, the fundamental computational frameworks for doing so using the Johnson–Cook and Preston–Tonks–Wallace plasticity models. Modeled single-particle impact morphology outputs were compared with experimental microstructures using scanning electron microscopy and optical microscopy. The computed von Mises flow stresses associated with the two plasticity models were compared with traditionally static nanoindentation data as well as dynamic spherical nanoindentation stress–strain curves. Continued work with the finite element analysis framework developed herein will enable the best cold spray parameters to be identified for optimized antimicrobial properties as a function of deformation-mediated microstructures while still maintaining the structural integrity of the deposited material. Subsequent work will extend the finite element analysis models to multi-particle impacts when spray-dried and gas-atomized copper powder particles have been appropriately meshed.

Keywords antimicrobial coatings · antipathogenic surfaces · cold spray · copper · contact killing and inactivation · finite element analysis · Johnson–Cook · nanoindentation · Preston–Tonks–Wallace · single-particle impact analysis

✉ Jeremy Schreiber
jms5532@arl.psu.edu

Kristin Sundberg
kristinsundberg7@yahoo.com

Danielle L. Cote
dlcote2@wpi.edu

1 Raytheon Technologies, Waltham, MA 02451, USA

2 Materials Science and Engineering, Worcester Polytechnic Institute, Worcester, MA 01609, USA

3 Applied Research Laboratory, Pennsylvania State University, State College, PA 16801, USA

4 Solvus Global LLC, 104 Prescott St, Worcester, MA 01605, USA

Introduction

Copper cold spray coatings and material consolidations have been found to have greater antimicrobial effectiveness than that of other common thermal spray methods, such as wire arc spray deposition and plasma spray deposition (Ref 1). Upon observing the increased antimicrobial efficacy associated with copper cold spray surfaces, the enhanced rate of contact killing and inactivation has been attributed to the significant particle impact velocity related to the cold spray process (ranging from 600 to 1000 m s^{-1}) (Ref 2, 3), which in turn yields severely plastically deformed microstructures that contain numerable atomic ion diffusion pathways. In turn, this paper builds off of prior work reported in (Ref 4) as well as subsequent work detailed in

(Ref 5-10). Prior work used nanostructured spray-dried particulate feedstock as well as conventionally gas-atomized copper powder feedstock during the high-pressure cold spray process to form antipathogenic solid-state copper coatings that were deposited upon alloyed aluminum substrates. After using *Staphylococcus aureus* bacteria to test the bactericidal properties of the conventional copper cold-sprayed coatings relative to the two thermally sprayed samples already mentioned, the nanostructured and conventional copper cold-sprayed surfaces were tested for antiviral contact inactivation of the influenza A virus. After 2 h of exposure to the copper cold-sprayed surfaces, per an Environmental Protection Agency (EPA) benchmark, the surviving influenza A virus was assayed, and the results were compared with one another.

The results showed that the nanostructured copper surface more effectively reduced the percentage of active influenza A virions than that of the conventional copper coating. The difference in microstructure between the two coatings is one of the main factors affecting antimicrobial properties, where the nanostructured antipathogenic surface maintains a much smaller grain size and, therefore, a higher percentage of grain boundaries in a given surface area, which act as diffusion pathways than the conventional copper cold-sprayed surfaces. Given the identification of the respective microstructures as being one of the main contributing factors associated with antipathogenic efficacy, as well as the fact that mechanical properties may be directly linked to a material's microstructure, computational modeling can be used to link the influence of the cold sprayable powder and the influence of cold spray-processing parameters to the resultant microstructures and subsequent antimicrobial properties. Linkages made in terms of the structure-processing-properties-performance paradigm of materials science and engineering, which are achieved through computational modeling, will enable optimal antimicrobial performance to be actualized.

Continued optimization of contact killing/inactivating surfaces is important for combating the growing problem of antibiotic resistance as well as preventing contact fomite transmission from high-touch surfaces in hospital environments. Models can be used to determine the best cold spray parameters to use for the optimization of antimicrobial properties, while still maintaining the structural integrity of the material, and may aid in the development of a robust understanding of copper contact killing mechanisms associated with bacterial agents and copper contact inactivating mechanisms associated with viral pathogens. For more information surrounding the prospective mechanisms associated with copper contact killing/inactivation, the reader should refer to (Ref 11-13). This work aims to set a baseline for modeling of the copper cold spray deposition process by first studying single-particle impact phenomena associated with conventional copper cold spray systems. Future modeling work will build upon this model wherein nanostructured copper cold spray processing and single-particle impact phenomena will be explored. That being said, this paper includes some preliminary experimental data associated with the nanostructured copper powder/coating to show the microstructural and mechanical differences between the conventional and nanostructured materials. Ultimately, this same data will be used in follow-on work to model nanostructured copper cold spray single-particle and multi-particle impact phenomena.

Background

Two models based in Abaqus finite element analysis (FEA) software were considered: the Johnson–Cook plasticity model (JC) and the Preston–Tonks–Wallace (PTW) constitutive model. Both models are high-strain-rate plasticity models that can be adapted to take inputs from cold spray processing parameters and output temperature evolution associated with particle–substrate impact, particle velocity upon impact, the von Mises flow stress, the plastic equivalent strain, and particle–substrate deformation morphology data. The von Mises flow stress can be thought of as either being at least equivalent to the minimum tensile stress required for the onset of yielding, which would be the yield strength of the material. On the other hand, if the von Mises flow stress output is found to notably exceed an appropriate tensile yield stress of a given material, then it may also be thought of as the flow stress required to continue the process of yielding until reaching the ultimate tensile stress. In other words, the post-yield point von Mises flow stress may be understood as the stress required to enable continued elastoplastic and plastic deformation for a given material, see (Ref 14), when the ultimate tensile stress is reached.

The JC plasticity model has been in use since the 1980 s and breaks down above strain rates greater than 10^5 s^{-1}. On the other hand, the PTW constitutive model is newer and benefits from the fact that it does not rely on empirical materials models and data, but rather relies upon thermodynamic principles and can, therefore, provide accurate plasticity behavior from 10^{-3} to 10^{13} s^{-1} strain rates. However, the same FEA meshing constraints apply for both models, making it difficult to model nanostructured materials. As alluded to already, this paper inspects the single-particle impact phenomena associated with conventional copper powder deformation during cold spray processing with both the JC and PTW models. For additional information surrounding the implementation of said FEA models or nuanced nature of the JC and PTW models the reader should refer to (Ref 14-16).

To validate the modeled flow stress outputs, modeled strain values can be used in Hollomon's power law equation to determine the output stress for copper, in accordance with (Ref 17, 18), with the following equation,

$$\sigma = K\varepsilon^n,$$

where K is the strength coefficient for annealed copper with a value of 315 MPa, ε is the modeled strain output, and n is the strain hardening exponent for copper with a value of 0.54. The power law does not account for strain rate, making it a tool to estimate the general magnitude of the modeled flow stress outputs. Further materials microstructure and mechanical testing were of course needed to understand model validity and single-particle impact response.

For the impact of a single copper particle, there are morphologies/microstructures specific to the cold spray process including particle deformation and dynamic recrystallization, jetting, and substrate-particle interlocking. Needless to say, single-particle deformation is associated with the high-impact velocities attributed to the cold spray process. For copper powder propelled in a carrier gas toward a static alloyed aluminum substrate, the copper powder's momentum is transferred, at least in part, upon impact in the form of kinetic energy to the surrounding substrate, thus causing plastic deformation. In simplified terms, jetting is observed alongside the severe plastic deformation at the particle/substrate interface where material from the particle and/or substrate experience an ejective flow along the upper regions of the particle–substrate interfacial edges, as has been reported upon in (Ref 14, 19, 20).

Nanoindentation can be used alongside microstructural examination to capture the hardness at a given load or depth as well as resultant mechanical property data that can be coupled with the JC and PTW models. Static nanoindentation test data using a Berkovich tip can be converted to a Vickers Hardness Number (VHN) through a geometrical relationship where the projected cross-sectional area of a Berkovich tip at a given depth matches the area of a Vickers indenter tip at the same depth. The derived equation is given as follows, in accordance with (Ref 21-23), such that

$$H_v = 0.0945(H_{\mathrm{NI}}),$$

where H_v is the VHN an H_{NI} is the nanoindentation hardness at a given load and/or depth with units of MPa. In any case, H_{NI} can also be converted to a yield strength. An empirical relationship has been developed for bulk cold-worked copper alloys for both the yield strength, σ_y, and the ultimate tensile strength, σ_u, that takes into account the effects of cold working and strain hardening on the yield strength of a material, as discussed in (Ref 24), such that,

$$\sigma_y = 2.874(H_{\mathrm{NI}})$$

and

$$\sigma_u = 3.353(H_{\mathrm{NI}}).$$

As a function of strain, the flow stress, σ_f, will range from σ_y and σ_u in accordance with the stress required to continue yielding during deformation until the σ_u is reached.

Nanoindentation systems may also be refocused from static/conventional Berkovich testing toward alternative tip geometries as well as alternative testing protocols to evaluate mechanical properties beyond hardness. By way of considering nanoindentation protocols that expand in the direction of measurable properties other than hardness and the modulus of elasticity, for example, one will benefit from the ability to overcome the need for empirically derived strength–hardness relations. Such empirically derived strength–hardness relations may not be truly suitable for a given task since the material data used to formulate the relations may not reflect the composition, microstructure, or processing condition of a material under consideration. Those who turn toward advanced nanomechanical methods will also benefit by way of avoiding Berkovich-related indentation size effect (ISE) strain gradient plasticity effects when attempting to evaluate a given material (Ref 25). That is not to say that alternative modes of analysis and nanomechanical inspection are free of limitations. Rather, many of the limitations typically associated with the use of more recent nanoindentation testing methods are readily overcome.

For instance, when an advanced dynamic or continuous stiffness measurement (CSM)-based approach is coupled with a cono-spherical nanoindenter tip geometry, CSM-induced errors can be accounted for as detailed in (Ref 26), tip radii can be varied to prevent or account for any spherical ISE's according to (Ref 27), and if we accept the claims and approaches taken to date, which is not a trivial decision, then effective zero points can be derived and introduced to account for superficial sample surface artifacts and the limited ability of the device to detect the true point of initial contact as laid out in (Ref 28-31). With the aforementioned in mind, the use of a cono-spherical diamond nanoindenter tip coupled with the CSM methodology enables elastic, elastoplastic, and plastic deformation to be captured through the evaluation of nanoindentation stress–strain curves. While numerable nanoindentation stress–strain curve evaluation techniques have been presented within the relevant academic literature, which can be found in (Ref 5, 31-37), the most recently refined approach established by Leitner et al. has emerged as one of the most theoretically consistent approach to date (Ref 33). In fact, turning to the Leitner et al. refinements enable a near one-

to-one comparison with data obtained through traditional tensile testing. As such, the nanoindentation stress–strain curves provide a robust method for yield and ultimate tensile strength determination, which may be coupled with the JC and PTW computational outputs in so far as the von Mises flow stresses are concerned.

In short, this work uses JC and PTW models for single-particle impact of conventional gas-atomized copper powder on an alloyed aluminum substrate. Model outputs of flow stress and deformation morphology are compared to measured microstructures and mechanical properties. Follow-on work must be undertaken to model the single-particle impact of spray-dried copper powder and the effects of multi-particle impact. Creating a relationship between cold spray parameters and resultant material properties will allow for future optimization of copper cold spray coatings, including the improvement of conventional copper cold spray coatings' antimicrobial properties.

Methods and Materials

Cold Spray Consolidation

Conventional and nanostructured copper cold spray coatings of 0.5-mm thicknesses were consolidated upon aluminum substrates. The gas-atomized copper powder, which was used to produce the conventional copper cold spray coating, was sourced from Praxair, Inc. (Danbury, CT, USA). The spray-dried copper powder, utilized for the consolidation of the nanostructured copper cold spray coatings, was procured from Eltron Research & Development, Inc. (Boulder, CO, USA). The nanostructured powder was made via spray drying, where copper nanoparticles ranging 60 nm to 80 nm in diameter were encapsulated in a pure and ultra-fine/fine-grained metallic copper binder. The average particle diameter of the nanostructured copper powder was 25 μm, whereas the gas-atomized copper powder maintained a size range of -31/+ 5 μm. Scanning electron microscopy (SEM) was utilized to capture micrographs of the spray-dried as well as gas-atomized powders used during the course of this work, as shown in Fig. 1.

Fast-Rastered Single-Particle Deposits

The VRC Gen III MAX cold spray system (Box Elder, SD, USA) at the Pennsylvania State University (PSU) Applied Research Laboratory (University Park, PA, USA) was used to deposit individual gas-atomized copper particles onto four 1.00 inch by 6.00 inch by 1/8 inch thick Al 6061 substrates. Said single-particle deposits were achieved by way of fast-rastering, that is, quickly moving the cold spray

nozzle from side-to-side relative to the substrate, resulting in single-particle deposits for experimental analysis in support of the FEA work. The gas-atomized pure copper powder used during fast-rastering had a 20-μm average particle diameter and was directly sourced from PSU. While the gas-atomized powder utilized for the production of the conventional copper cold spray consolidated samples was not sourced from the same vendor associated with the PSU "fast-raster" powder, the PSU copper powder closely resembled the Praxair, Inc., copper powder. Due to availability and cost associated with acquiring the spray-dried feedstock particulates, the nanostructured copper powder was not deposited by way of a the fast-raster approach.

On the Powder Utilized

To clarify, three powders were utilized during the course of this research. To generate the consolidated nanostructured copper cold spray coatings the spray-dried feedstock from Eltron Research & Development, Inc., was utilized. To generate the consolidated conventional copper cold spray coatings, the gas-atomized feedstock from Praxair, Inc., was utilized. After retaining some of the Praxair, Inc., pure copper for microscopy-based analysis and nanoindentation analysis, all of the remaining pure copper gas-atomized feedstock from Praxair, Inc., was used to generate the copper cold spray coating during the course of the work. Accordingly, another gas-atomized copper feedstock with the same commercial purity and stored at PSU was used to generate the fast-rastered samples. Given the similar age of the feedstock, similar storage conditions, and equivalent powder purity, a degree of confidence underpinned the use of the copper feedstock from PSU to supplement the consolidated copper cold-sprayed coatings with comparable single-particle impacts.

Mechanical Properties

Static nanoindentation was performed with the Keysight Technologies Nano Indenter G200 system (Santa Rosa, CA, USA). The G200 system was utilized to indent powder, single-particle deposits, and cross-sectionally oriented (relative to the spray direction) consolidated cold spray coatings that are deposited using the gas-atomized as well as spray-dried feedstocks. Dynamic nanoindentation was performed using the iNano with an InForce 50 mN actuator from Nanomechanics, Inc. (Oak Ridge, TN, USA), now KLA Instruments, which is part of the KLA Corporation (Milpitas, CA, USA). This was applied to the consolidated cross sections for both conventional and nanostructured copper cold spray coatings as well. The G200 system was equipped with a Berkovich-shaped diamond nanoindenter tip from Micro Star Technologies, Inc. (Huntsville, TX,

Fig. 1 (a) and (b) are SEM micrographs of the spray-dried copper powder, while (c) and (d) are SEM micrographs of the gas-atomized copper powder. The scale bar associated with (c) is the same for (a) and the scale bar associated with (d) is the same for (b)
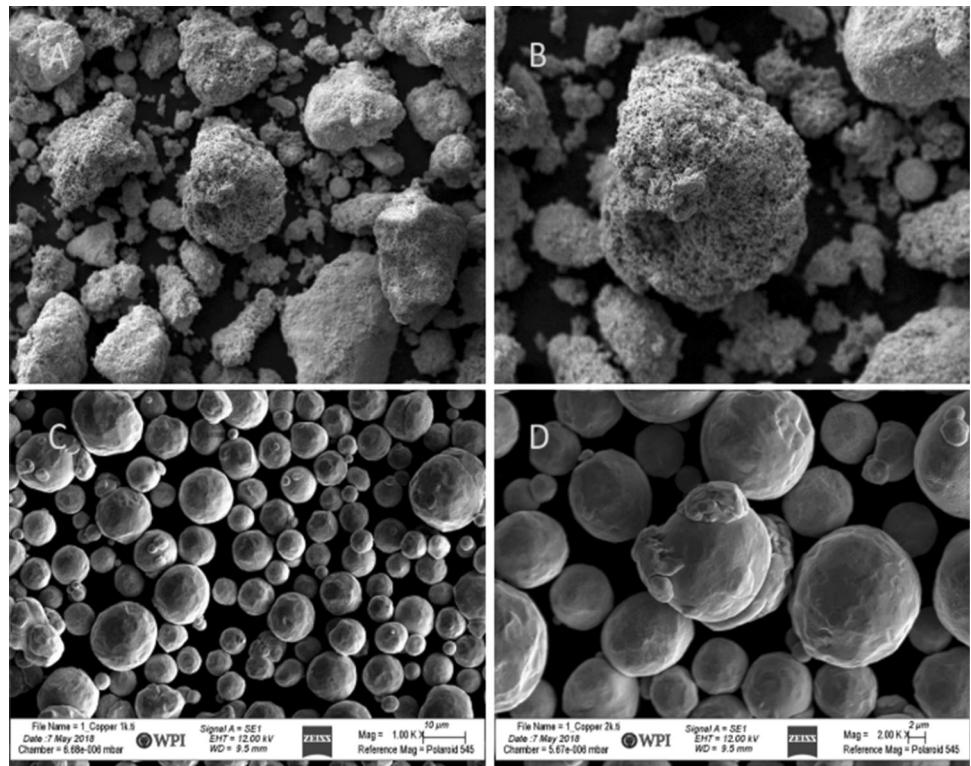
USA). For dynamic/CSM testing, a cono-spherical diamond nanoindenter tip from Synton-MDP LTD (Switzerland) was acquired. The cono-spherical indenter tip radius was 2.1 μm.

All of the nanoindentation samples were mounted and prepared according to standard metallurgical procedures prior to nanoindentation testing. The hardness of the powder was determined after testing 30 different powder particles of a similar diameter and were cross-sectionally prepared during the process of mounting and polishing. 5-by-5 indent arrays were performed upon each of the powder particles. 5-by-5 arrays were also carried out when the G200 nanoindentation system was utilized to characterize the consolidated samples. For static nanoindentation measurements of the conventional gas-atomized copper single-particle deposits and also for both the static and dynamic nanoindentation testing of the consolidated conventional and nanostructured copper, the coatings were oriented such that the indenter tip was normal to the coating-substrate interface, as seen in Fig. 2.

Microstructural Analysis

The powders and cold spray samples were mounted using the SimpliMet 4000 Mounting Press system from Buehler (Lake Bluff, IL, USA) with a phenolic powder. The standard procedure, as defined by Buehler, was used to prepare the samples with the mounting press and phenolic powder

with a heating time of 4 min, a cooling time of 3.5 min, a pressure of 4400 psi, and a temperature of 360° F. Prior to mounting, consolidated samples were first cut using a band saw and subsequently cut using an IsoMet High Speed Pro Precision Cutting Saw from Buehler for a cleaner cut with minimal residual stress accumulation. Specifically, the IsoMet saw was used to prepare the single-particle deposits described. For the powders and the coatings, a final 0.05-μm surface finish was achieved using a Struers, Inc., Tegramin-20 automatic polisher (Cleveland, OH, USA), a colloidal silica suspension and an appropriate polishing pad. Thereafter, the samples were ultrasonically cleaned in ethanol and immediately dried using compressed air.

SEM micrographs were obtained using a tungsten filament source-based SEM from ZEISS (Oberkochen, Germany). The specific SEM was a tabletop EVO-MA10 series. Accelerating voltages of 10 kV to 15 kV were utilized. SEM micrographs of powder were taken from both mounted powder cross sections and loose powder that was dispersed onto double-sided SEM mounting tape. Consolidated samples were cross-sectioned and mounted. Both secondary electron micrographs and backscattered electron micrographs were taken. After initial analysis in the SEM, samples were chemically etched to reveal the polycrystalline grain structure using a 25% nitric acid to 75% deionized water solution, then re-analyzed in the SEM. Optical micrographs of the single-particle deposit cross sections were obtained using an Inverted Metallurgical

Fig. 2 Optical micrographs of pre/post-static nanoindentation arrays associated with the nanostructured cold spray copper coatings, in (c) and (d), and the conventional cold spray copper coatings, in (a) and (b)
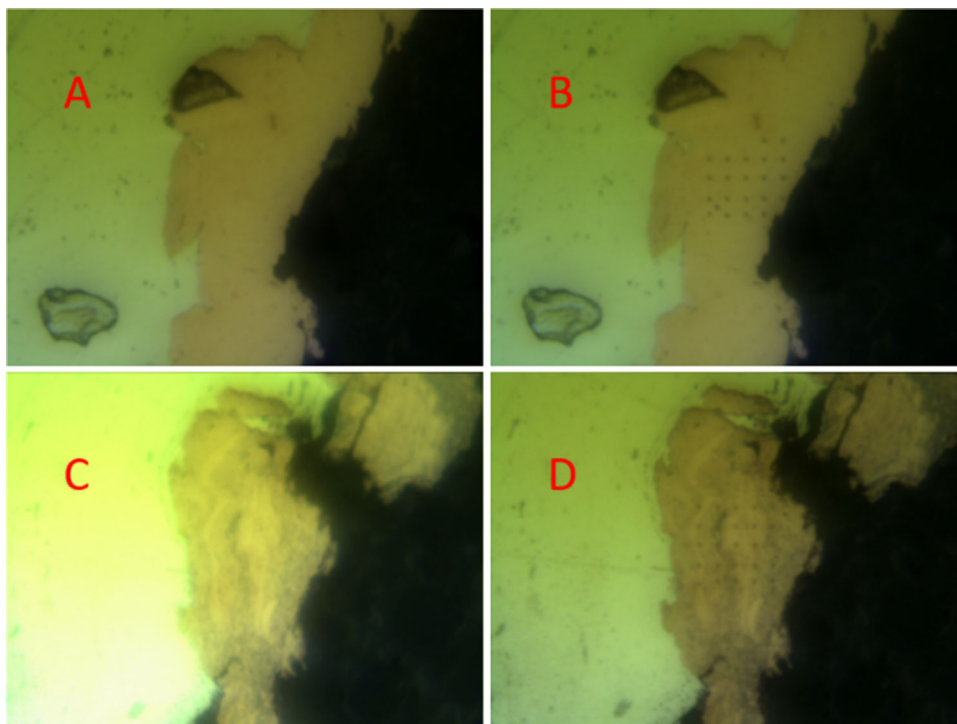
Microscope GX71 from the Olympus Corporation (Shinjuku City, Tokyo, Japan). The optical micrographs were captured using the Stream Essentials image analysis software, which was also sourced from Olympus.

Computational Modeling

The FEM's were developed using Abaqus CAE 2017 (Dassault Systemes SE, Vélizy-Villacoublay, France). The substrate size was assumed to be 1000 μm by 1000 μm by 250 μm to allow computed stresses to propagate freely without having to modify boundary conditions. Other assumptions include the particle and contact distance. The in silico particle and substrate were placed in near contact with one another with the substrate being fixed in three dimensions. The particle was given a predefined velocity and temperature prior to impact. The predefined inputs originate from simulation software protocols developed at PSU.

For a 25-μm particle sprayed with nitrogen at 450 °C and 500 psi, or 34.47 bar, the estimated particle temperature at impact was 210 °C and the estimated velocity at impact was 575 m s^{-1}. These parameters were based upon cold spray processing by way of a VRC Gen III MAX cold spray system. Model simulation time was set to 10^{-7} s, in order to capture the initial impact and rebound of the particles. Impact data were output at 10^{-9} s for suitable temporal resolution.

Contact definitions between the particle and the substrate are very important to properly simulate the deformation process. The kinematic contact method was used with the finite sliding formulation in Abaqus. The normal impact behavior was set to hard contact, while allowing separation after contact. Both the particle and the substrate were meshed with hexahedral elements, type C3D8RT. Significant partitioning was required in order to mesh the particle with hexahedral elements. The particle contained 896 elements, while the substrate contained 10,404 elements. Figure 3 shows the meshed particle and substrate prior to impact. General elastic and thermal material properties for copper used for this analysis. Density was set to

Johnson–Cook Model

The software used for JC modeling was Abaqus CAE 2017. The JC equation is

$$\sigma_f = \left[A + B\varepsilon_p^n\right]\left[1 + C\ln\dot{\varepsilon}_p\right]\left[1 - T_H^m\right],$$

where ε_p is the amount of effective plastic strain in the system and $\dot{\varepsilon}_p$ is the normalized effective plastic strain rate. A, B, and C are experimentally determined material constants, where A is the quasi-steady-state yield stress, B is the power law pre-exponential factor, C is the strain rate pre-exponential factor, n is the strain hardening exponent, and m is the thermal softening exponent. T_H is a normalized temperature, given as

Fig. 3 FEA orientation and setup is provided on the left-hand side of this figure. The meshing assigned to the particle and substrate in silico prior to impact is provided on the right-hand side of this figure
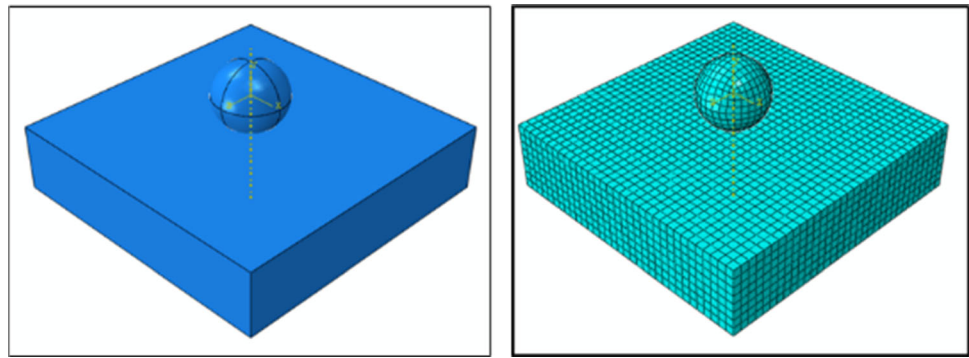
Table 1 General material constants used in the copper particle model

Young's modulus	Poisson's ratio	Density	Thermal conductivity	Inelastic heat fraction	Specific heat
110 GPa	0.343	8930 kg/m^3	385 W/m*K	0.9	385 J/kg*K

$$T_H = \frac{T - T_{\text{room}}}{T_{\text{melt}} - T_{\text{room}}}.$$

Finally, general material constants and constants defined by the JC model applied herein are tabulated in Tables 1 and 2 below and are in accordance with (Ref 38).

Table 2 JC material constants utilized

A	B	C	n	m	T_{melt}	T_{room}
300 MPa	292 MPa	0.025	0.31	1.09	1356° K	294° K

Preston–Tonks–Wallace Model

The software used for the PTW model was the same as that affiliated with the JC model. The PTW model was implemented into Abaqus using a Fortran VUHARD subroutine that overrides the standard plasticity models. The PTW equation is shown below, such that

$$\hat{\tau} = \hat{\tau}_s + \frac{1}{p}(s_0 - \hat{\tau}_y) \ln \left[1 - \left[1 - \exp\left(-p\frac{\hat{\tau}_s - \hat{\tau}_y}{s_0 - \hat{\tau}_y}\right) \right] \right.$$
$$\left. * \exp\left\{ -\frac{p\theta\psi}{(s_0 - \hat{\tau}_y)\left[\exp\left(p\frac{\hat{\tau}_s - \hat{\tau}_y}{s_0 - \hat{\tau}_y}\right) - 1\right]} \right\} \right],$$

where $\hat{\tau}$ is a dimensionless flow stress parameter, $\hat{\tau}_s$ and $\hat{\tau}_y$ are the thermal activation work hardening saturation stress and the yield stress, respectively. The equivalent plastic strain rate is represented by ψ, p is the density, θ is the saturation stress, and s_0 represents a material constant. Material properties were defined by PTW for copper in accordance with (Ref 16). Each material constant for copper is described and tabulated below in Table 3. Due to the excessive length of derivation, the constants listed below are not described in this paper but are described in (Ref 16).

Results and Discussion

Modeling

JC and PTW models were used to computationally analyze phenomena associated with single-particle impact behavior of gas-atomized copper cold sprayable powder particles. The velocity and temperature associated with particle impact as a function of time relative to initial impact of the particle with the substrate in silico using the JC model is presented in Fig. 4. Initial particle impact starts 3 ns to 4 ns from the origin of each graph and is most easily observed within the velocity versus time graph presented in Fig. 4(a) as the point at which the particle velocity begins to decrease steadily. The node selected for this output was at bottom dead center of the particle, and the same node was selected for each plot. The initial impact follows through to the 45 ns mark, at which point the particle becomes fully compressed. A slight increase in velocity after this point indicates some elastic rebound on the nodal level. The temperature versus time graph depicted in Fig. 4(b) shows that there is a continuous temperature increase upon impact due to particle deformation. The temperature band widens over time because of the noise attributed to nodal oscillation. A JC temperature plot for a cross section of a fully impacted gas-atomized copper particle is presented in Fig. 5.

Table 3 PTW material constants used

θ	p	s_0	s_∞	κ	γ		Y_0	y_∞
0.025	2.0	0.0085	0.00055	0.11	0.00001		0.0001	0.0001
Y_1	Y_2	β	G_0	α	α_p		M	C
0.094	0.575	0.25	510	0.20	0.43		63.54 m_u	0.3933 cm μs^{-1}
s	ρ_a	γ_a	G/B	ρ_o	Γ		g	k
1.50	8.933	2.0	0.35	9.02 g cm^{-3}	1.6×10^{-4} cal mol^{-1} K^{-2}		2/3	1.8 cal s^{-1} cm K
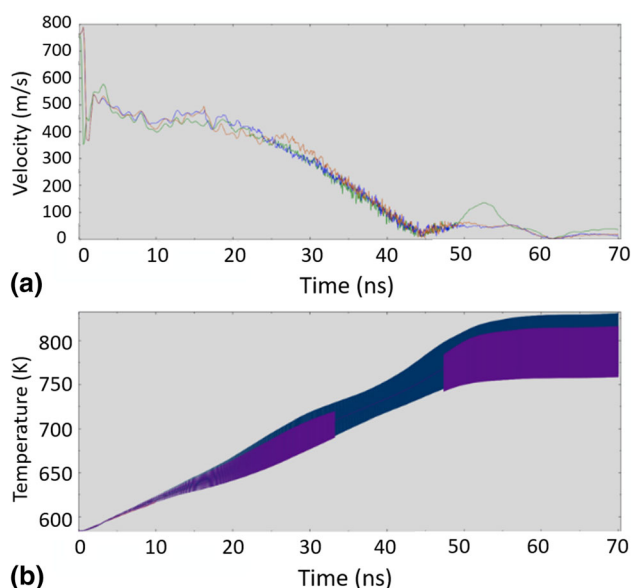
Fig. 4 Velocity versus time graph is depicted in (a). Temperature versus time graph is depicted in (b)

More to the point, the rendered temperature distribution plot in Fig. 5 captures the temperature profile of the particle at the maximum impact displacement prior to the onset of rebounding. At said point in time, the maximum contact pressure and peak temperature may be ascertained. The temperature profile reveals a significantly higher temperature at the particle/substrate interface versus the interior region of the particle. Such profiles are consistent with similar works, such as (Ref 39). This is supported by the von Mises stress profile following particle impact, as shown in Fig. 6, where the von Mises stress was also found to be highest at the particle/substrate interface. The increase in stress and temperature at the edges of the particle can be attributed to localized plastic deformation due to the high velocity of the particle on impact, which agrees with (Ref 20, 40). This increase in flow at the particle/substrate interface can contribute to jetting, which is captured hereafter.

JC temperature and stress profiles assist in pinpointing the conditions needed for metallurgical bonding and subsequent adhesion of the particle to the substrate. Additional work is needed for PTW profiles. That being said, in terms of the plastic equivalent strain (PEEQ) profiles at the point of final particle impact for both the JC and PTW models are provided in Fig. 7. Figure 7(a) and (b) show that the accumulated PEEQ strain at the particle/substrate interface is larger than in the center of the particle. This is consistent with (Ref 41) as well. Since strain captures how much work has been performed upon a particle during impact, PEEQ has a direct relationship to hardness. PEEQ values can be used to calculate flow stress by applying the values to the JC and PTW equations. The von Mises flow stress values for a fully impacted conventional copper powder particle are 367 MPa and 394 MPa for JC and PTW, respectively. These values were calculated directly from the JC and PTW equations. The larger PTW flow stress model correlates well with the PEEQ diagram, which shows PTW as having greater strains than that of the JC approach.

The general magnitude of the flow stress values can be validated by applying the modeled PTW strain rate of 1.109 s^{-1} to Hollomon's power law to get a flow stress output of 332 MPa. The power law value was found to be within the same magnitude of both the PTW and JC values. All three values are close to the values for flow stress of cold-worked copper found in industry. Compared to the JC model, the PTW model produces more accurate results. This is because the JC model is based on a "curve fit" of experimental data from prior work with bulk Al 6061 and has homologous input of temperature. On the other hand, PTW doesn't rely on empirical relations but does use widely accepted values based on bulk copper as the experimental data for single-particle deposits simulation and computation. Morphology comparison between JC and PTW outputs can be seen in Fig. 8 and 9, respectively.

The impacted particle morphologies captured in Fig. 8(a) through 8(d) are provided as a function of time. Specifically, Fig. 8(a) showcases the initial particle–substrate interaction upon single-particle impact in silico via FEA using the JC plasticity model 10 ns after initial particle–substrate contact was made. Next, Fig. 8(b) depicts the onset of extended plastic deformation at 20 ns after initial contact of the particle and substrate occurred. Particular attention should therefore be given to the

Fig. 5 The JC model temperature distribution profile associated with a fully impacted particle–substrate system is presented in this figure
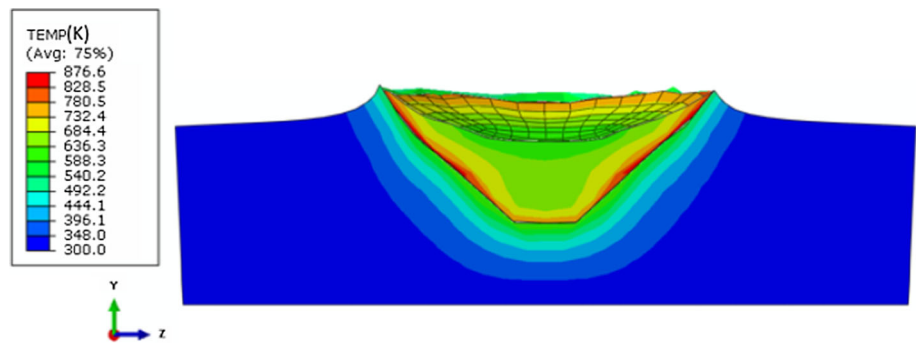
Fig. 6 The JC model von Mises flow stress distribution profile associated with a fully impacted particle–substrate system is presented in this figure
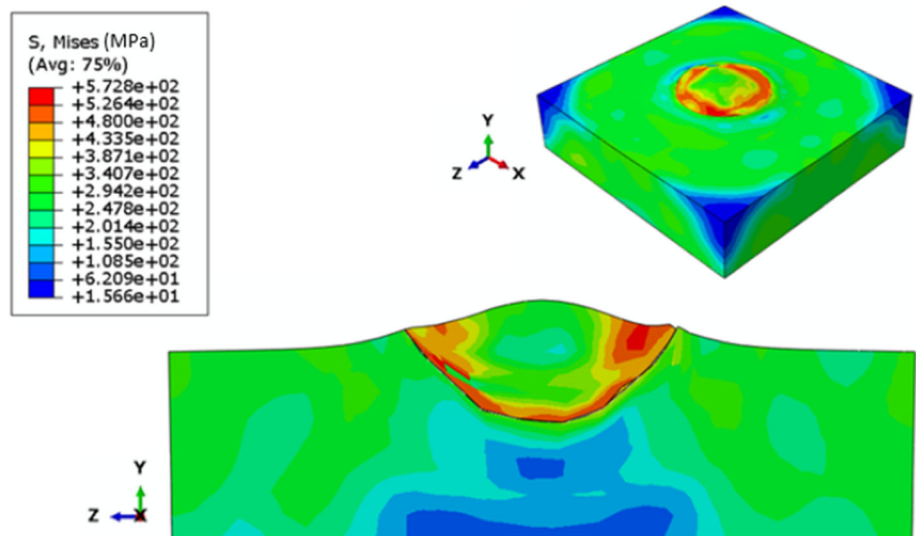

Fig. 7 The PEEQ profile associated with fully impacted particle–substrate system using the (a) JC model as well as the (b) PTW model during FEA computations
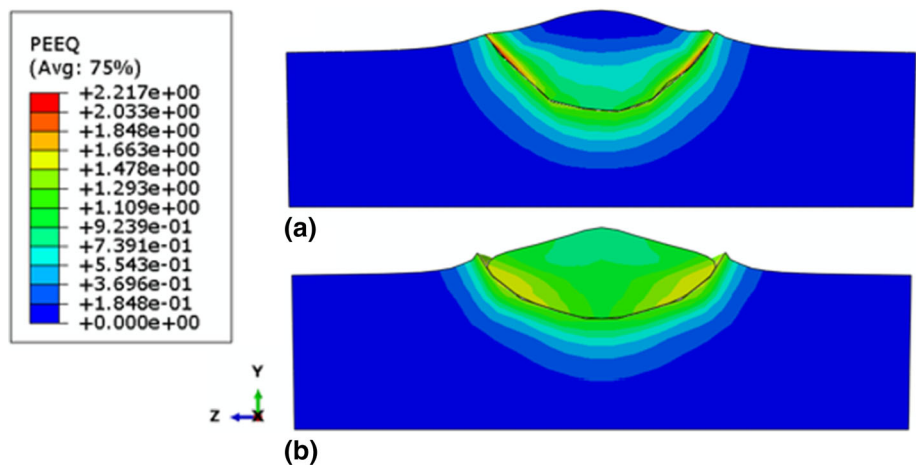

deformation occurring at the particle–substrate interface with respect to Fig. 8(b). In keeping with chronological analysis, Fig. 8(c) illustrates continued development of the highly strained particle–substrate interface, especially toward the surface of the substrate and at the outer peripheral edges of the particle–substrate interface, thus promoting jetting development and related phenomena prior to the 30 ns time mark. Lastly, Fig. 8(d), which corresponds with 40 ns time, reveals continued impacted particle flattening and enhanced jetting along said edges of the particle–substrate interfacial region. By Fig. 8(d), the outmost apexes of the jet appear to sharpen and also

Fig. 8 JC particle impact
morphologies at (a) 10 ns,
(b) 20 ns, (c) 30 ns, and
(d) 40 ns
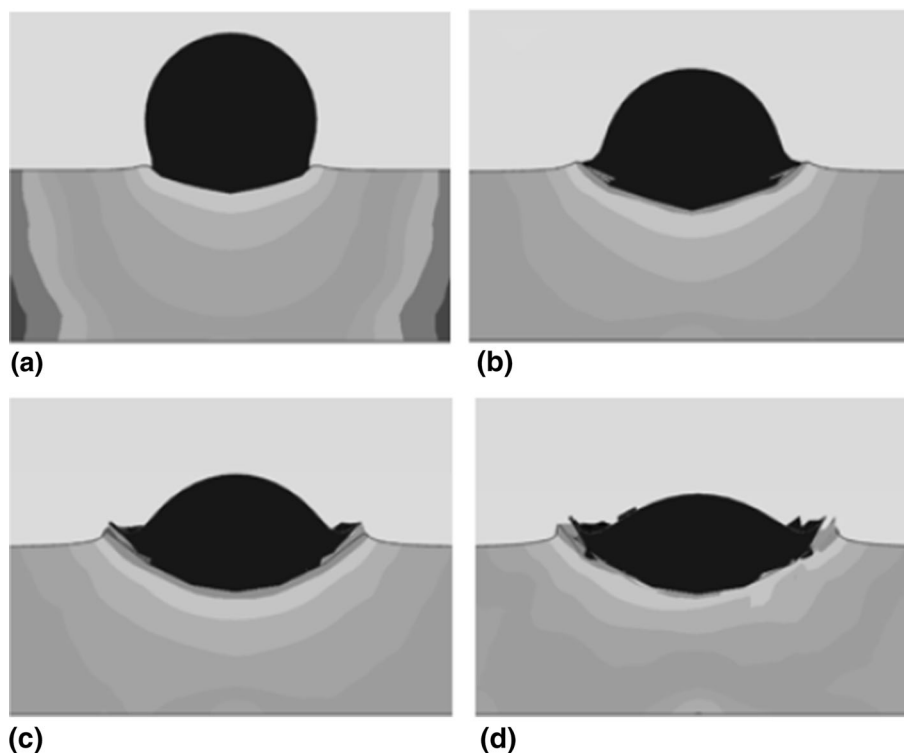
Fig. 9 PTW particle impact
morphologies at (a) 10 ns,
(b) 20 ns, (c) 30 ns, and
(d) 40 ns
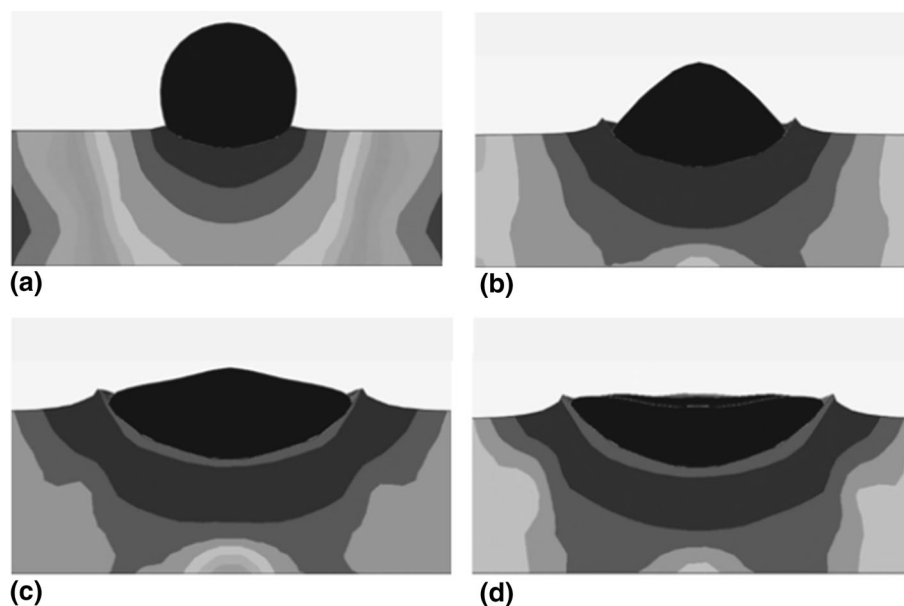
appears as though they are beginning to dissipate. This is a reflection on the limits of the JC model. As for Figure's 9(a) through 9(d), the PTW model-based renderings show similar morphologies but have more degrees of freedom to overcome the temporal resolution issues associated with the JC approach. However, both the JC and PTW models are mesh–based as well as constant volume models and more development and refinement is needed to model more complex powder structures like that of the spray-dried

copper powder utilized during the formation of the nanostructured copper cold spray coatings.

Mechanical Data

In large part, this subsection of the Results and Discussion focuses upon the nanoindentation behavior recorded, as well as the advanced nanomechanical assessment pursued, during the course of this research. The hardness of the

spray-dried powder was found to be at least 1.21 GPa, or 114 HVN. Since porosity analysis revealed the fact that the spray-dried powder was only 50% dense, as reported upon in (Ref 6), the precise hardness of cross-sectioned spray-dried copper powder must be expressed with the clarifier "at least" since the phenolic mounting material could very well have, at least in some cases, penetrated the powder during preparation. That being said, it is rather unlikely that the phenolic resin invaded the less dense regions of the spray-dried powder when Fig. 11(b) is considered. Future work will ensure that any hypothetical or prospective clarifiers are rendered unnecessary by way of applying dynamic microparticle compression testing to record mechanical properties of individual particulates without local effects. Furthermore, the energy-dispersive x-ray spectroscopy performed upon the mounted and cross-sectioned spray-dried copper particles, as reported upon in (Ref 6), also attests to the limited likelihood of mounting resin infiltration into the porous particles, which would have in turn caused a lower hardness to be recorded.

In so far as future work is concerned, it is extremely important that accurate and reliable mechanical characterization is achieved in order to define material-specific properties within forthcoming model refinements. For example, if the JC model is applied, robust mechanical assessment of a given particle will enable feedstock specific A, B and n values to be used over that of bulk values. As demonstrated by Assadi et al., the use of powder specific JC input parameters notably changes the temperature distribution during copper particle impact when parameters for a 33 μm particle are used versus the use of bulk values (Ref 39). Nevertheless, relative to the static hardness of the gas-atomized copper powder at a depth of 250 nm, which was found to be 1.31 GPa, or 123 HVN, the lower hardness of a 50% porous powder versus a nearly fully dense powder particle was found to be consistent with particle strength properties as a function of porosity reported upon in (Ref 42).

In light of the prior solidification modeling reported upon in (Ref 6) for an average particle diameter of 25 μm (given the use of 25 μm during modeling and single-particle deposition at PSU), the effective grain size is 2.23 μm in diameter. By way of using this value we may call upon the Hall–Petch relationship for copper where

$$\sigma_y = \sigma_o + kd^{-0.5},$$

such that σ_y is the yield strength, σ_o and k are material-specific constants, and d is the grain size. From the work of Gertsman et al., we know that σ_o, in MPa, is 92 ± 12, k, in MPa $\mu m^{0.5}$, is 399 ± 61, and d is in units of μm (Ref 43). As a result, we may compare the nanoindentation hardness-based yield strength, derived using Tabor's relation, with the yield strength obtained from the Hall–Petch relation.

Due to the ISE, it was unsurprising to find that the hardness-derived yield strength was 422.58 MPa, for the gas-atomized powder, which was slightly greater than the upper bound (306.34 MPa to 412.04 MPa) associated with the Hall–Petch relation given above. Nevertheless, the slight difference with the upper bound of the Hall–Petch yield strength and the hardness-derived value is commendable given the limited nanoindentation depth that can be achieved when testing a stiff particle mounted in a compliment mounting material before the mounting material begins to influence the measured properties as addressed in (Ref 44).

The hardness value for the single-particle deposit was found to be greater than that of the gas-atomized powder as well as the consolidated conventional copper cold spray sample. Specifically, the single-particle deposit achieved a static nanoindentation hardness of 2.03 GPa, or 191 HVN, while the hardness of the conventional copper cold spray coating was 1.75 GPa, or 165 HVN. This may be attributable to the use of different powder in the single-particle deposit process. While the powder provided by PSU was made of pure copper and was gas-atomized too, it is possible that the atomizing gas used in the process affected the resultant microstructure, potentially making the PSU copper powder harder than that of the Praxair, Inc., powder. Prior work substantiates the fact that atomizing gas species can affect the resultant microstructure of the gas-atomized powder as discussed in (Ref 45, 46). On the other hand, in Fig. 4, there is a notable increase in temperature from particle friction and impact with the substrate. This increase in temperature, coupled with the mechanical stress associated with particle impact, can affect dynamic recrystallization and subsequent hardness values as mentioned in (Ref 47). Therefore, it is also possible that the dynamic recrystallization from severe plastic deformation, intrinsic to the cold spray process, would have a greater effect on a single particle than a coating due to the effects of thermal softening and dislocation annihilation as recrystallized subgrains are nucleated from multi-particle impacts, which is complimented by (Ref 48, 49). Regardless, the consolidated conventional copper cold spray coatings' hardness was consistent with other work discussed in the literature, such as (Ref 50).

Concerning the hardness of the nanostructured copper cold spray coating, which was found to be 2.41 GPa, or 226 HVN, relative to the hardness of the conventional copper cold spray coating, the greater hardness of the nanostructured consolidation follows from the virtually fully dense and nano-grained microstructure. At the same time, the cold spray process causes powders to compress upon impact, thus densifying the initially porous spray-dried copper powder particles during processing, which enables the nanostructured microstructure to dictate the mechanical

behavior rather than its' as spray-dried porosity. This densification is largely due to the effects of work hardening from the tampering or shot peening effect of particles during impact as they build upon each other. (Ref 51), among other earlier works, concur with this interpretation.

The dynamic nanoindentation hardness of nanostructured copper cold spray coating was found to be 2.48 GPa while the modulus of elasticity was found to be 61.3 GPa. In comparison, the consolidated conventional copper cold spray coatings' dynamic nanoindentation hardness was 1.79 GPa, whereas its' modulus of elasticity was found to be 62.92 GPa. The two hardness's are highly consistent with the static nanoindentation values reported above, providing a degree of assurance that the hardness achieved through CSM-based protocols were not artificially hardened by the CSM process itself as has been observed in other materials according to (Ref 52). Moreover, the trend noted above surrounding the magnitude of the hardness of the nanostructured coating relative to the conventional cold spray coating remains in the case of dynamic nanoindentation testing too. Again, the nanostructured copper maintained a greater hardness than the conventional copper due to the finer grain size, as supported by the Hall–Petch relationship, which states that grain-boundary strengthening, and the subsequent material yield strength, increases with decreasing grain size (Ref 43, 53).

Concerning hardness, Tuckerman said it well when he affirmed that hardness is "a hazily conceived conglomeration or aggregate of properties of a material, more or less related to each other" in (Ref 52). That is to say, indentation hardness values are not an intrinsic material property and therefore do not provide vital discernments into a material's performance under tensile stresses and strains. Accordingly, nanoindentation scholars have improved upon the array of mechanical responses that can be assessed. Thus, advanced dynamic spherical nanoindentation stress–strain curve determination has emerged and at the same time endures ongoing improvements such that said curves may serve as a trustworthy substitute to customary tensile testing methods. The essential refinements developed by Leitner et al. in (Ref 33) were employed herein for the purpose of determining nanoindentation stress–strain curves for the nanostructured as well as conventional copper cold spray coatings. Additional information on calculations may be found in (Ref 6) and (Ref 5). Figure 10 presents the mechanical flow curves of each of the coatings studied via advanced dynamic spherical nanoindentation.

In explicit terms, the advanced dynamic spherical nanoindentation stress–strain curve presented in Fig. 10 shares remarkable agreement with the single-particle impact von Misses flow stress outputs. The consolidated conventional copper cold spray coating was found to have a yield strength approximately equal to 350 MPa as

indicated through annotation of Fig. 10. Considering the fact that this is greater than the Hollomon power law-derived flow stress of 332 MPa for a single-particle impact output assuming bulk copper properties at a PTW strain rate of 1.109, the slightly higher nanomechanical yield stress of approximately 350 MPa is noteworthy. At the same time, the slightly lower yield strength experimentally acquired relative to the von Misses flow stress values for a fully impacted gas-atomized particle in silico (367 MPa for the JC model and 394 for the PTW model) is consistent with the same phenomena cited earlier in regards to slight copper softening associated with multi-particle and multi-layered cold spray impacts.

With the aforementioned details in mind, we have achieved a degree of confidence surrounding the implementation of a FEA infrastructure which achieves outputs consistent with experimentally assessed data for comparable processing parameters and conditions. As a result, we will be able to readily pursue the previously mentioned future work that will apply the computational FEA JC and FEA PTW models to the spray-dried feedstock once a proper meshing approach is actualized. Additionally, the baseline nanostructured spherical nanoindentation stress–strain curve and approximate yield strength of at least 810 MPa will enable rapid prototyping of FEA implementations of proximal meshes that must be utilized to study single-particle impact phenomena associated with the spray-dried powder as well. Furthermore, the experimentally substantiated FEA approach taken herein for gas-atomized copper will also be able to execute a vast combination of various processing parameter values to identify the cold spray processing procedure that is best able to achieve desired impact deformation behavior. Concerning the desirability of particle deformation, the processing parameters that compute particle deformation known to be indicative of the microstructures that would maximize the number of diffusion pathways for contact killing/inactivation will be procured for optimal antipathogenic performance of conventionally cold-sprayed copper coatings too.

Microstructural Considerations

Microstructural analysis was used to validate the measured mechanical behavior, and the explanations assigned to the mechanical observations made relative to one another, as well as the single-particle impact morphologies obtained from the FEA models. Cross sections of both the gas-atomized and spray-dried powder are shown in Fig. 11. There was a clear difference in microstructure between the two powders, specifically with the spray-dried copper powder having much smaller particles within the powder structure, as we would expect considering the varied production methods used. The consolidated conventional and
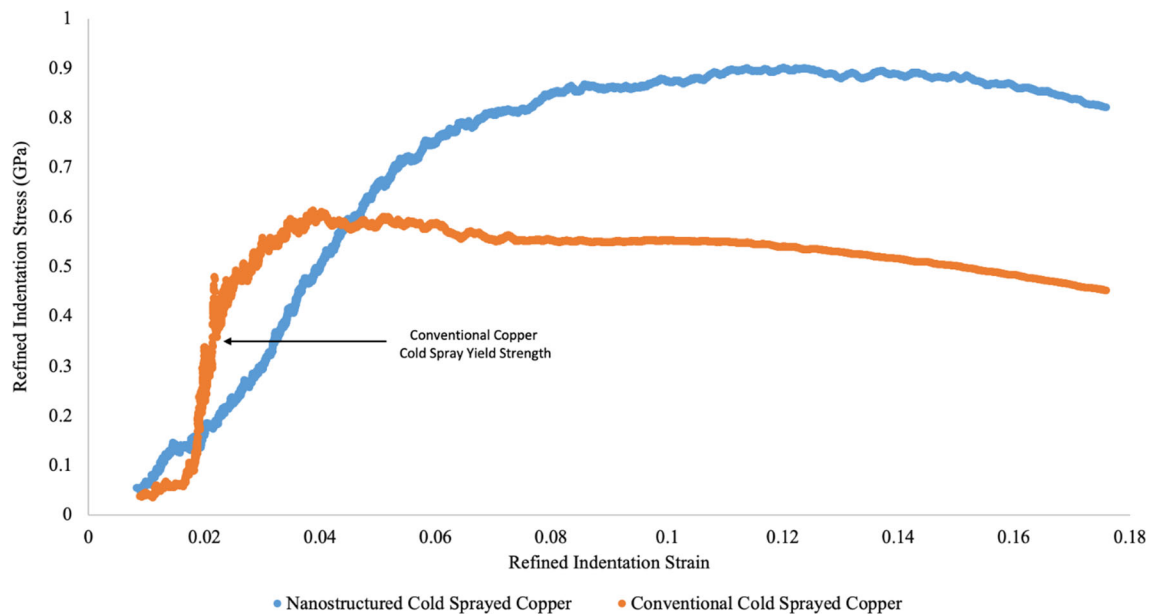
Fig. 10 The spherical dynamic stress–strain curve for the nanostructured copper cold spray coating (blue curve) as well as the conventional copper cold spray coating (orange curve)
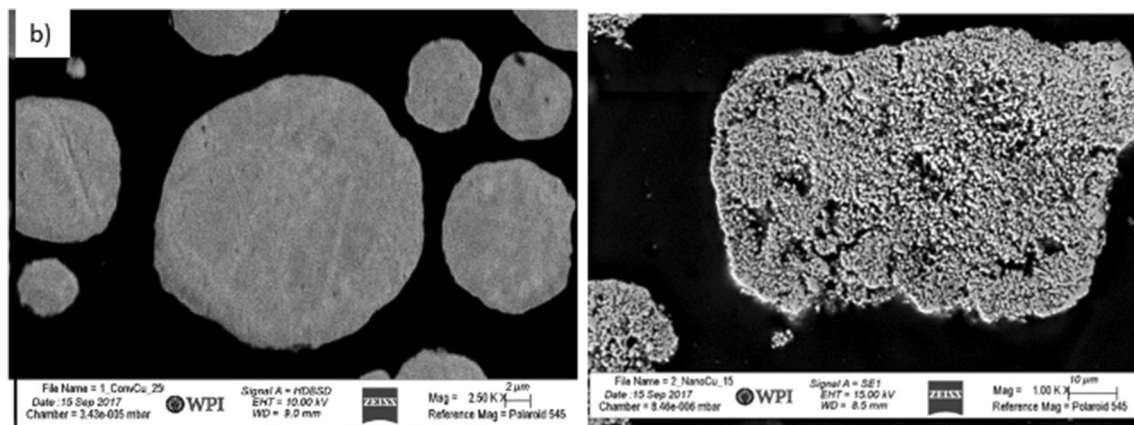

Fig. 11 SEM micrographs of gas-atomized (Left) and spray-dried powder (Right)

nanostructured copper coatings can be observed in Fig. 12. The conventional copper cold spray sample maintains much larger grains than that of the nanostructured copper specimen. The nanoscale grain size of the nanostructured copper coatings qualitatively validates the higher hardness values from the Hall–Petch relationship, where there is a relationship between smaller grain size and increased material strength according to (Ref 53).

To appreciate the complimentary nature between the modeled impact and produced single-particle deposit, Fig. 13 couples the FEA simulation output impact morphology for a conventionally gas-atomized copper powder particle with the experimentally obtained single-particle impact morphology. This shows the once spherical powder particle has undergone elongation perpendicular to the

direction of impact in a similar manner to that identified in (Ref 54). The two arrows in Fig. 13 highlight the comparable jetting observed computationally and experimentally. The computationally modeled single-particle deposit morphology was complimented by the fast-rastered single-particle deposits analyzed and presented in Fig. 13.

Magnification of the coating/substrate interface in Fig. 14 allows for comparison of the jetting phenomena associated with the copper cold spray coating(s), the single-particle deposit, and the particle impact model. In Fig. 14, it can be seen that the particles are no longer spherical and are compressed parallel to the substrate. At the particle/substrate interface, intermixing, which is characteristic of the cold spray process, is evident. It is more difficult to see jetting in consolidated coatings due to the high degree
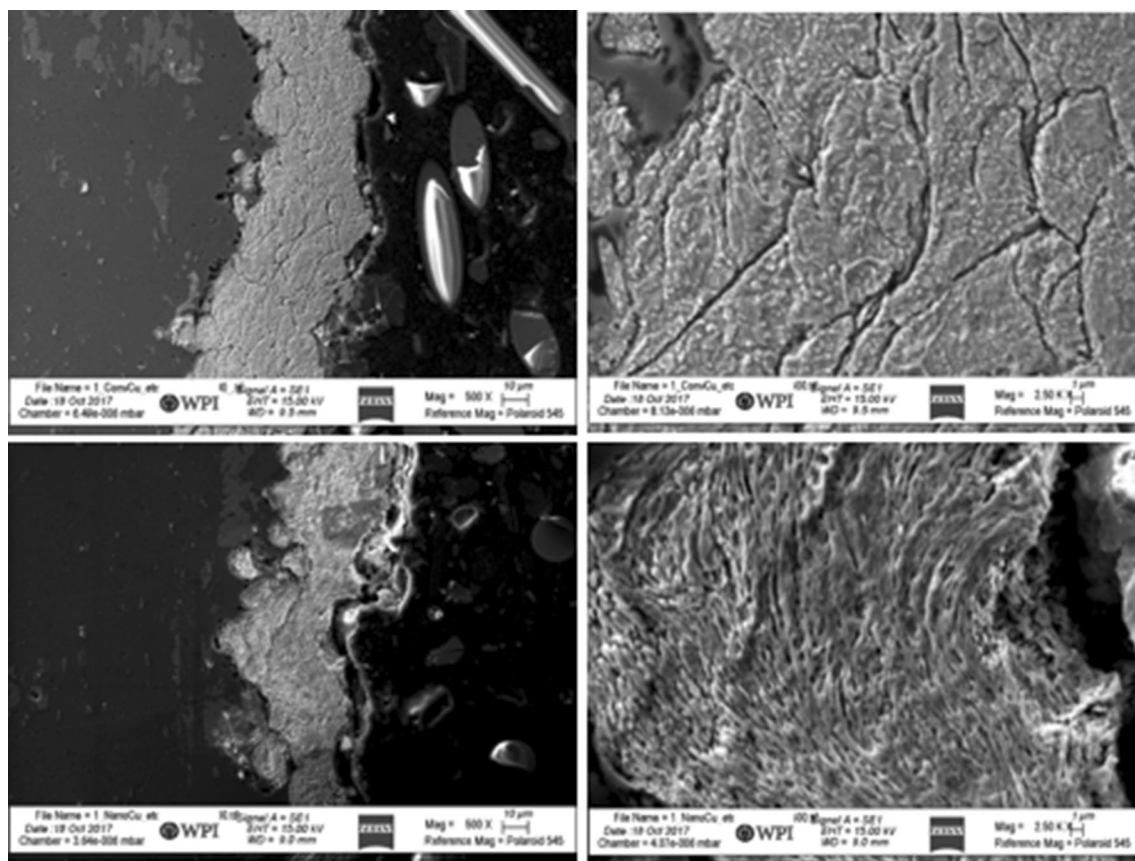
Fig. 12 The consolidated conventional (Top row) and nanostructured copper (Bottom row) coatings can be observed in the cross-sectional orientation relative to the spray direction

Fig. 13 FEA simulation output impact morphology (Left) for a conventionally gas-atomized copper powder particle with the experimentally obtained single-particle impact morphology (Right)
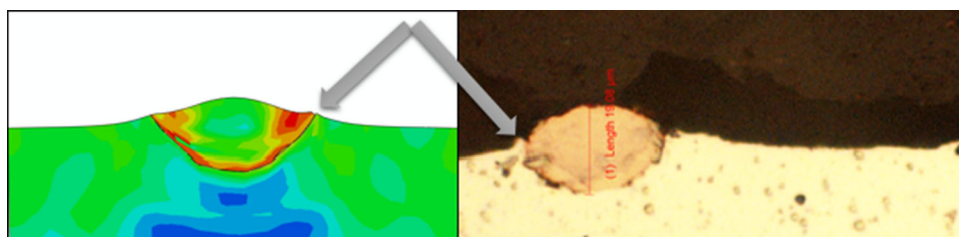

of plastic deformation and multi-particle impacts which often interacts with the jet structure as has previously been recognized in (Ref 41, 50, 54). Knowing the grain structure of copper cold spray coatings not only allows for validation of the model and hardness measurements, but also provides a steppingstone for future modeling of nanostructured copper, in a manner that is consistent with the ethos of the work presented in (Ref 55).

Conclusion

Compared with microstructural analysis as well as nanomechanical property assessment and hardness/modulus measurements, FEA single-particle impact models were

developed for antimicrobial copper cold spray applications. One of the FEA models assumed the JC model while the other called upon the PTW model. Accordingly, we may draw the following conclusions:

- The JC and PTW model outputs for the von Misses flow stress was found to be on the same order of magnitude as the Hollomon power law calculation, industrial values for cold-worked copper, and the yield strength obtained experimentally using an advanced dynamic spherical nanoindentation stress–strain curve protocol.

- Jetting observed in the JC and PTW FEA morphological outputs from the computational models was found to be consistent with the optical micrograph obtained
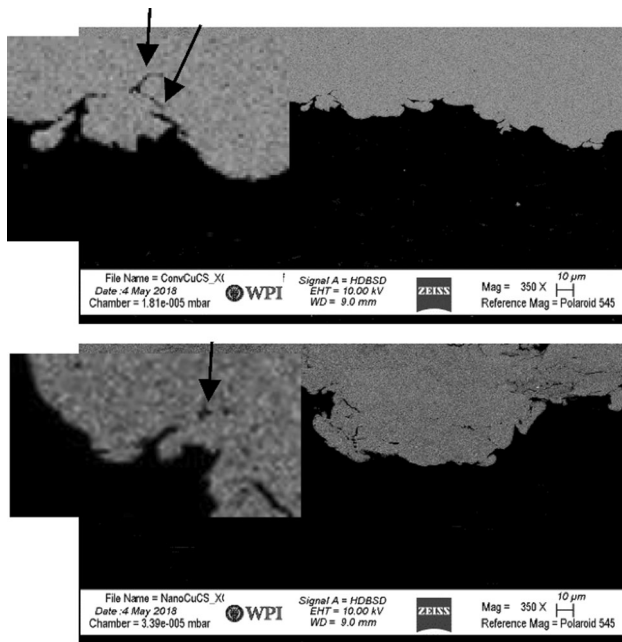
Fig. 14 SEM micrographs of the conventional copper coating (Top row) vs. the nanostructured copper coating (Bottom row) are presented herein

for a single copper particle deposit onto an Al 6061 substrate material. Remnants of material that underwent jetting was also observable within the consolidated copper cold spray coatings.

- By way of analyzing the single-particle impact morphologies as a function of time and associated with the JC model output and PTW model output revealed the fact that the PTW model is more accurate than the JC model. The dependency upon thermodynamic underpinning of the PTW model enables more accurate FEA computations.

- To conclude, this work has developed a baseline for optimizing the cold spray process for improved antipathogenic performance.

References

1. V.K. Champagne and D.J. Helfrich, A Demonstration of the Antimicrobial Effectiveness of Various Copper Surfaces, *J. Biol. Eng.*, 2013, **7**(1), p 8

2. C. Massar, K. Tsaknopoulos, B.C. Sousa, J. Grubbs, and D.L. Cote, Heat Treatment of Recycled Battlefield Stainless-Steel Scrap for Cold Spray Applications, *JOM*, 2020, **72**, p 3080-3089

3. B.C. Sousa, C.E. Walde, V.K. Champagne, and D.L. Cote, Initial Observation of Grain Orientation Dependent Nanoindentation

4. Hardness of Al 6061 Gas-Atomized Powder, *Int. J. Metall. Met. Phys.*, 2020, **5**(1), p 050

5. K. Sundberg and V. Champagne, Effectiveness of Nanomaterial Copper Cold Spray Surfaces on Inactivation of Influenza A Virus, *J. Biotechnol. Biomater.*, 2015, **05**(04), p 1

6. B. Sousa, K. Sundberg, C. Massar, V. Champagne, and D. Cote, *Spherical Nanomechanical Characterization of Novel Nanocrystalline Cu Cold Spray Manufactured Materials*, Vol 2019, 2019

7. B.C. Sousa, K.L. Sundberg, M.A. Gleason, and D.L. Cote, Understanding the Antipathogenic Performance of Nanostructured and Conventional Copper Cold Spray Material Consolidations and Coated Surfaces, *Crystals*, 2020, **10**(6), p 504

8. K. Sundberg, *Application of Materials Characterization, Efficacy Testing, and Modeling Methods on Copper Cold Spray Coatings for Optimized Antimicrobial Properties*, Worcester Polytechnic Institute, Worcester, 2019

9. K. Sundberg, The Effect of Corrosion on Conventional and Nanomaterial Copper Cold Spray Surfaces for Antimicrobial Applications, *Biomed. J. Sci. Tech. Res.*, 2019, **22**(3), p 16753-16763

10. K. Sundberg, M. Gleason, B. Haddad, V.K. Champagne, C. Brown, R.D. Sisson, and D. Cote, The Effect of Nano-Scale Surface Roughness on Copper Cold Spray Inactivation of Influenza A Virus, *Int. J. Nanotechnol. Med. Eng.*, 2019, **4**, p 33-40

11. O. Mishchenko, V. Filatova, M. Vasylyev, V. Deineka, and M. Pogorielov, Chemical and Structural Characterization of Sandlasted Surface of Dental Implant Using ZrO_2 Particle with Different Shape, *Coatings*, 2019, **9**(4), p 223

12. F.-P. Lee, D.-J. Wang, L.-K. Chen, C.-M. Kung, Y.-C. Wu, K.-L. Ou, and C.-H. Yu, Antibacterial Nanostructured Composite Films for Biomedical Applications: Microstructural Characteristics, *Biocompatibility, and Antibacterial Mechanisms, Biofouling*, 2013, **29**(3), p 295-305

13. J.O. Noyce, H. Michels, and C.W. Keevil, Inactivation of Influenza A Virus on Copper versus Stainless Steel Surfaces, *Appl. Environ. Microbiol.*, 2007, **73**(8), p 2748-2750

14. C.E. Santo, N. Taudte, D.H. Nies, and G. Grass, Contribution of Copper Ion Resistance to Survival of Escherichia Coli on Metallic Copper Surfaces, *Appl. Environ. Microbiol.*, 2008, **74**(4), p 977-986

15. J.M. Schreiber, *Finite Element Implementation of the Preston–Tonks–Wallace Plasticity Model and Energy Based Bonding Parameter for the Cold Spray Process*, Pennsylvania State University, State College, 2016

16. G.R. Johnson and W.H. Cook, Fracture Characteristics of Three Metals Subjected to Various Strains, Strain Rates, Temperatures and Pressures, *Eng. Fract. Mech.*, 1985, **21**(1), p 31-48

17. D.L. Preston, D.L. Tonks, and D.C. Wallace, Model of Plastic Deformation for Extreme Loading Conditions, *J. Appl. Phys.*, 2003, **93**(1), p 211-220

18. S. Kardes and C. Choi, Determining the Flow Stress Curve with Yield and Ultimate Tensile Strengths. Pt.I: Important Data from the Tensile Test, *Stamp. J.*, 2011, Retrieved from https://www.thefabricator.com/stampingjournal/article/metalsmaterials/

19. S. Kardes and C. Choi, Determining the Flow Stress Curve with Yield and Ultimate Tensile Strengths. Pt.II: Using the Curve for FE Simulation, *Stamp. J.*, 2011, Retrieved from https://www.thefabricator.com/stampingjournal/article/metalsmaterials/

20. M. Grujicic, J.R. Saylor, D.E. Beasley, W.S. DeRosset, and D. Helfrich, Computational Analysis of the Interfacial Bonding between Feed-Powder Particles and the Substrate in the Cold-Gas Dynamic-Spray Process, *Appl. Surf. Sci.*, 2003, **219**(3–4), p 211-227

21. P.C. King, G. Bae, S.H. Zahiri, M. Jahedi, and C. Lee, An Experimental and Finite Element Study of Cold Spray Copper

Impact onto Two Aluminum Substrates, *J. Therm. Spray Technol.*, 2010, **19**(3), p 620-634

21. E. Broitman, Indentation Hardness Measurements at Macro-, Micro-, and Nanoscale: A Critical Overview, *Tribol. Lett.*, 2017, **65**(1), p 23

22. W.C. Oliver and G.M. Pharr, An Improved Technique for Determining Hardness and Elastic Modulus Using Load and Displacement Sensing Indentation Experiments, *J. Mater. Res.*, 1992, **7**(6), p 1564-1583

23. J. Hay, Introduction to Instrumented Indentation Testing, *Exp. Tech.*, 2009, **33**(6), p 66-72

24. S.C. Krishna, N.K. Gangwar, A.K. Jha, and B. Pant, On the Prediction of Strength from Hardness for Copper Alloys, *J. Mater.*, 2013, **2013**, p 1-6

25. W.D. Nix and H. Gao, Indentation Size Effects in Crystalline Materials: A Law for Strain Gradient Plasticity, *J. Mech. Phys. Solids*, 1998, **46**(3), p 411-425

26. S.J. Vachhani, R.D. Doherty, and S.R. Kalidindi, Effect of the Continuous Stiffness Measurement on the Mechanical Properties Extracted Using Spherical Nanoindentation, *Acta Mater.*, 2013, **61**(10), p 3744-3751

27. J.K. Engels, S. Gao, W. Amin, A. Biswas, A. Kostka, N. Vajragupta, and A. Hartmaier, Indentation Size Effects in Spherical Nanoindentation Analyzed by Experiment and Non-Local Crystal Plasticity, *Materialia*, 2018, **3**, p 21-30

28. S.R. Kalidindi and S. Pathak, Determination of the Effective Zero-Point and the Extraction of Spherical Nanoindentation Stress-Strain Curves, *Acta Mater.*, 2008, **56**(14), p 3523-3532

29. S. Pathak, J. Shaffer, and S. Kalidindi, Determination of an Effective Zero-Point and Extraction of Indentation Stress-Strain Curves without the Continuous Stiffness Measurement Signal, *Scr. Mater.*, 2009, **60**(6), p 439-442

30. A.J. Moseson, S. Basu, and M.W. Barsoum, Determination of the Effective Zero Point of Contact for Spherical Nanoindentation, *J. Mater. Res.*, 2008, **23**(1), p 204-209

31. S. Pathak, Development and Validation of a Novel Data Analysis Procedure for Spherical Nanoindentation, *PhD. thesis, Drexel University*, (2009)

32. S. Pathak and S.R. Kalidindi, Spherical Nanoindentation Stress–Strain Curves, *Mater. Sci. Eng. R Rep.*, 2015, **91**, p 1-36

33. A. Leitner, V. Maier-Kiener, and D. Kiener, Essential Refinements of Spherical Nanoindentation Protocols for the Reliable Determination of Mechanical Flow Curves, *Mater. Des.*, 2018, **146**, p 69-80

34. P. Chivavibul, M. Watanabe, S. Kuroda, J. Kawakita, M. Komatsu, K. Sato, and J. Kitamura, Effects of Particle Strength of Feedstock Powders on Properties of Warm-Sprayed WC-Co Coatings, *J. Therm. Spray Technol.*, 2011, **20**(5), p 1098-1109

35. L.H. He and M.V. Swain, Nanoindentation Derived Stress–Strain Properties of Dental Materials, *Dent. Mater.*, 2007, **23**(7), p 814-821

36. J. Dean, J.M. Wheeler, and T.W. Clyne, Use of Quasi-Static Nanoindentation Data to Obtain Stress–Strain Characteristics for Metallic Materials, *Acta Mater.*, 2010, **58**(10), p 3613-3623

37. S. Basu, A. Moseson, and M.W. Barsoum, On the Determination of Spherical Nanoindentation Stress–Strain Curves, *J. Mater. Res.*, 2006, **21**(10), p 2628-2637

38. G.R. Johnson and W.H. Cook, A Constitutive Model and Data from Metals Subjected to Large Strains, High Strain Rates and High Temperatures, in *Proceedings of 7th International Symposium on Ballistics, The Hague, Netherlands* (1983)

39. H. Assadi, I. Irkhin, H. Gutzmann, F. Gärtner, M. Schulze, M. Villa Vidaller, and T. Klassen, Determination of Plastic Constitutive Properties of Microparticles through Single Particle Compression, *Adv. Powder Technol.*, 2015, **26**(6), p 1544-1554

40. W. Li, K. Yang, D. Zhang, and X. Zhou, Residual Stress Analysis of Cold-Sprayed Copper Coatings by Numerical Simulation, *J. Therm. Spray Technol.*, 2016, **25**(1–2), p 131-142

41. L. Venkatesh, N.M. Chavan, and G. Sundararajan, The Influence of Powder Particle Velocity and Microstructure on the Properties of Cold Sprayed Copper Coatings, *J. Therm. Spray Technol.*, 2011, **20**(5), p 1009-1021

42. P. Chivavibul, M. Watanabe, S. Kuroda, J. Kawakita, M. Komatsu, K. Sato, and J. Kitamura, Effects of Particle Strength of Feedstock Powders on Properties of Warm-Sprayed WC-Co Coatings, *J. Therm. Spray Technol.* (2011)

43. V.Y. Gertsman, M. Hoffmann, H. Gleiter, and R. Birringer, The Study of Grain Size Dependence of Yield Stress of Copper for a Wide Grain Size Range, *Acta Metall. Mater.*, 1994, **42**(10), p 3539-3544

44. W. Yan, C.L. Pun, and G.P. Simon, Conditions of Applying Oliver–Pharr Method to the Nanoindentation of Particles in Composites, *Compos. Sci. Technol.*, 2012, **72**(10), p 1147-1152

45. G. Antipas, Gas Atomization of Aluminium Melts: Comparison of Analytical Models, *Metals (Basel)*, 2012, **2**(2), p 202-210

46. A. Ünal, Effect of Processing Variables on Particle Size in Gas Atomization of Rapidly Solidified Aluminium Powders, *Mater. Sci. Technol.*, 1987, **3**(12), p 1029-1039

47. J. Villafuerte, Modern Cold Spray, *Modern Cold Spray: Materials, Process, and Applications*, J. Villafuerte, Ed., Springer, Cham, 2015,

48. M.R. Rokni, C.A. Widener, and V.R. Champagne, Microstructural Evolution of 6061 Aluminum Gas-Atomized Powder and High-Pressure Cold-Sprayed Deposition, *J. Therm. Spray Technol.*, 2014, **23**(3), p 514-524

49. S. Yin, X. Wang, X. Suo, H. Liao, Z. Guo, W. Li, and C. Coddet, Deposition Behavior of Thermally Softened Copper Particles in Cold Spraying, *Acta Mater.*, 2013, **61**(14), p 5105-5118

50. C. Borchers, F. Gärtner, T. Stoltenhoff, H. Assadi, and H. Kreye, Microstructural and Macroscopic Properties of Cold Sprayed Copper Coatings, *J. Appl. Phys.*, 2003, **93**(12), p 10064-10070

51. R. Jenkins, S. Yin, B. Aldwell, M. Meyer, and R. Lupoi, New Insights into the In-Process Densification Mechanism of Cold Spray Al Coatings: Low Deposition Efficiency Induced Densification, *J. Mater. Sci. Technol.*, 2019, **35**(3), p 427-431

52. A. Leitner, V. Maier-Kiener, and D. Kiener, Dynamic Nanoindentation Testing: Is There an Influence on a Material's Hardness?, *Mater. Res. Lett.*, 2017, **5**(7), p 486-493

53. N. Hansen, Hall-Petch Relation and Boundary Strengthening, *Scr. Mater.*, 2004, **51**(8), p 801-806

54. Y.-K. Kim, K.-S. Kim, H.-J. Kim, C.-H. Park, and K.-A. Lee, Microstructure and Room Temperature Compressive Deformation Behavior of Cold-Sprayed High-Strength Cu Bulk Material, *J. Therm. Spray Technol.*, 2017, **26**(7), p 1498-1508

55. M.P. Schmitt, J.M. Schreiber, A.K. Rai, T.J. Eden, and D.E. Wolfe, Development and Optimization of Tailored Composite TBC Design Architectures for Improved Erosion Durability, *J. Therm. Spray Technol.*, 2017, **26**(6), p 1062-1075